Optoelectrode based on fiber Fabry-Perot cavity functionalized by conductive indium tin oxide

Meng Luo[a], Xinyu Chang[a], Danheng Gao[a], Xingyue Wen[a], Pingping Teng[a], Jiabao Zhu[a], Hongyu Ma[a], Aohua Li[a], Xinghua Yang[a],*, Kang Li[b], Nigel Copner[b], Zheng Zhu[a],*

[a]Key Laboratory of In-Fiber Integrated Optics, Ministry of Education, College of Science, Harbin

Engineering University, Harbin 150001, China

[b]Wireless & Optoelectronics Research & Innovation Centre, Faculty of Computing, Engineering &

Science, University of South Wales, Wales, CF37 1DL, UK

Fax: 0086-451-82519850

Phone: 0086-451-82519850

E-mail: * yangxh@hrbeu.edu.cn; zhuzheng@hrbeu.edu.cn

Abstract

In this paper, an F-P interferometer optoelectrode structure functionalized by conductive indium tin oxide (ITO) thin film is first proposed. When the F-P cavity is filled with electrolyte, the effective refractive index in the cavity can be modulated by applying an electrical potential to form an electric double layer on the interface of the electrolyte and electrode. Significantly, this work presents a novel structure of integrated F-P interferometer optoelectrode functionalized by conductive ITO to measure the conductivity of the electrolyte. And it is the first time to use interference spectrum to react the conductivity of solution, which provides a new method for conductivity detection. This simple preparation, convenient operation, and low-costed optical fiber F-P interference optoelectrode has great potential in the biochemical analysis, biosensing, electrochemical analysis and battery electrode surface monitoring.

1. Introduction

Conductivity measurement of the interface of electrode and electrolyte solutions is of great importance in academic research, industrial production applications, and microbial chemistry research [1-3]. Previously, several conductivity measurement methods have been reported. Some of these assays are conductivity analysis, capacitive coupling, capillary electrophoresis, etc. [1-5]. However, to the best of our knowledge, conductivity detection has not been combined with optical fiber FPI sensing.

With the rapid development of optical fiber technology, micro-nano optical fiber technology is widely used in the sensing field [6-8]. Among them, optical fiber interferometer has been intensively studied and widely used in the detection of physical parameters, biological macromolecules, heavy metal ions, and various gas components [9-11]. Among them, the optical fiber Fabry-Perot interferometer (FPI) is widely used in confining spaces and special environments [12-17]. Moreover, as the research progresses, the application of functional material integrated with optical fiber draws more and more attention. For example, material coatings such as gold nanoparticles, black scales, and graphene oxide, materials are widely used in the field of fiber optic sensing [18-21]. Among the materials that may be applied, indium tin oxide (ITO) is an interesting choice as a metal oxide semiconductor with not only low resistivity but also a high refractive index and high optical transparency.

In this paper, an online, simple-to-prepare FPI optoelectrode is first proposed. The integrated optoelectrode was prepared by integrating conductive ITO thin film electrode with an FPI. The optoelectrode is based on the effect of conductivity on the electric double layer between the electrode surface and the solution [22-25], which causes the effective refractive index to change near the transparent oxide electrode [26]. Results show that by combining the transparent ITO with the optical fiber FPI, the sensor exhibits high sensitivity to conductivity. Significantly, this integrated optical fiber on-line conductivity probe has great potentials in the fields of biochemical analysis, battery electrode surface monitoring, biosensing and academic research.

2. Experiment

2.1 Preparation process of the optical fiber FPI functionalized by ITO

In the study, the 3 dB coupler and single-mode fiber (SMF) used to make the interferometer were purchased from Yangtze Optical Fibre and Cable Joint Stock Limited Company. The diameter of the SMF is 125μm, and the core diameter is about 8μm. The optical fiber FPI was fabricated by the fiber largely offset misalignment fusion splicing method. Firstly, the 3 dB coupler and the SMF were fusion spliced with largely offset misalignment. The offset distance was 73 μm. Secondly, the single-mode fiber was cut to 150 μm (that is the length of the F-P cavity). Thirdly, the cut fiber and the SMF were fusion spliced with largely offset dislocation again, as shown in Fig. 1(a). Here, the optical fiber dislocation welding was carried manually using a commercial fusion splicer (JL KL-260B) in order to keep the two large intentional lateral offsets at the opposite offset direction. To ensure the alignment of the two optical fibers, we can perform the second offset fusion under the monitoring of the optical spectrum analyzer (OSA). In other words, a clear interference spectrum can be generated on the OSA screen. And, if the cavity length of FPI is less than 180 μm, the whole FPI structure can be seen on the screen of the fusion splicer, which is more helpful for us to adjust the position of the fiber to ensure that the direction

of the two fibers is aligned. Moreover, the splicing program we selected was the SMF-SMF splicing program with adjustment parameters: predischarge current of 65 units, predischarge duration of 1200 ms, discharge current of 85 units, discharge duration of 2000 ms.

Here, the cavity length of 150 μm was chosen for this experiment because the cavity length of the fiber FPI does not affect its RI sensitivity [28]. In addition, during the fabrication of the optical fiber FPI, the maximum optical fiber cavity length of 180um can be seen on the screen of the optical fiber fusion splicer. Too long cavity length is not easy to observe the actual state of the bias point in the welding process. Too short cavity length is not easy to cut. Therefore, the cavity length size of 150um was chosen in this experiment.
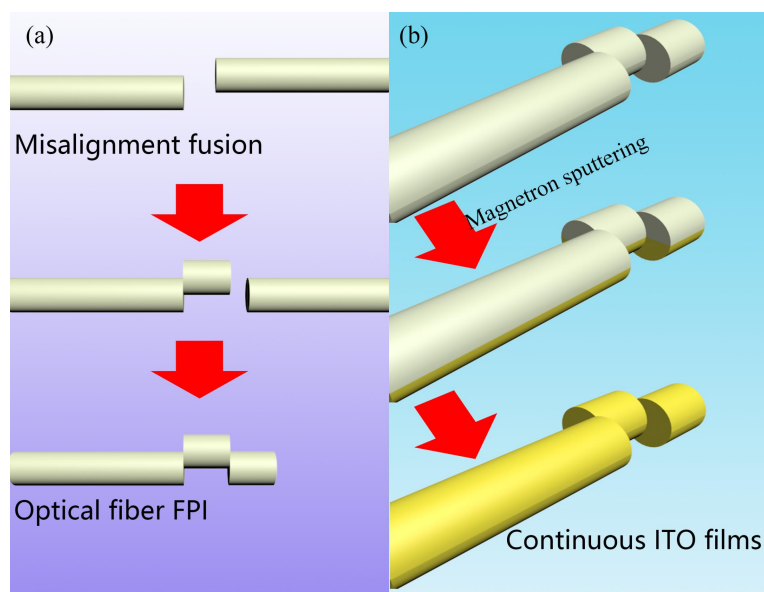

Fig. 1. Schematic diagram of the preparation of optical fiber FPI functionalized by ITO. (a) The preparation process of optical fiber FPI. (b) The preparation process of ITO film.

Fig. 1(b) shows the fabrication process of the optical fiber FPI-ITO. After finishing the fabrication of optical fiber FPI, the continuous ITO films were deposited on the FPI by radio frequency (RF) sputtering. Firstly, the fabricated optical fiber FPI was ultrasonically cleaned in water and ethanol. Then, it was sputtered twice by a commercially available RF magnetron sputtering system (JGP 450B). The optical fiber and the target were kept at an inclination angle of 30° during sputtering to ensure that the ITO was integrated on the end face of FPI. The thickness of the ITO film obtained by the above method is about 98 nm, which is measured by the 3D surface profiler (zygo), as shown in Fig. 2. When measuring film thickness, the sample surface is first pretreated and then coated with a gold film to increase reflection. And the difference between the maximum value and the minimum value is the ITO film thickness.
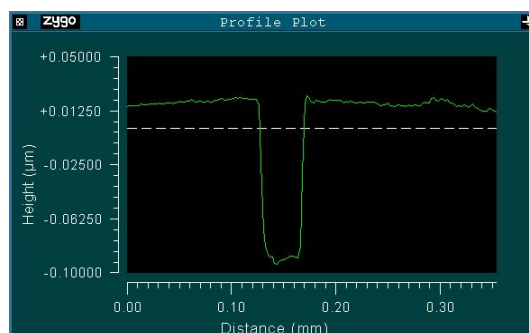
Fig. 2. Thickness of the ITO film measured on the upper surface of the fiber FPI.

Fig. 3(a)-(b) shows the scanning microscope (SEM, Thermo Fisher Apreo C) images of different magnifications. From Fig. 3(a)-(b), the overall structure of the FPI and the smooth surface of the ITO film are shown. Here, it can be seen that the quality of ITO film is good. And the smooth surface is conducive to the interference spectrum. The X-ray energy dispersive spectroscopy (EDS, Oxford) mapping images of different elements on the surface of the optical fiber FPI are shown in Fig. 3(c)-(f). In these figures, the distribution of O, In and Sn elements on the surface of the optical fiber FPI is shown, respectively. In and Sn elements are distributed almost exclusively on the fiber FPI surface, while the O element is also present on the substrate. This proves ITO thin film is distributed on the optical fiber FPI.
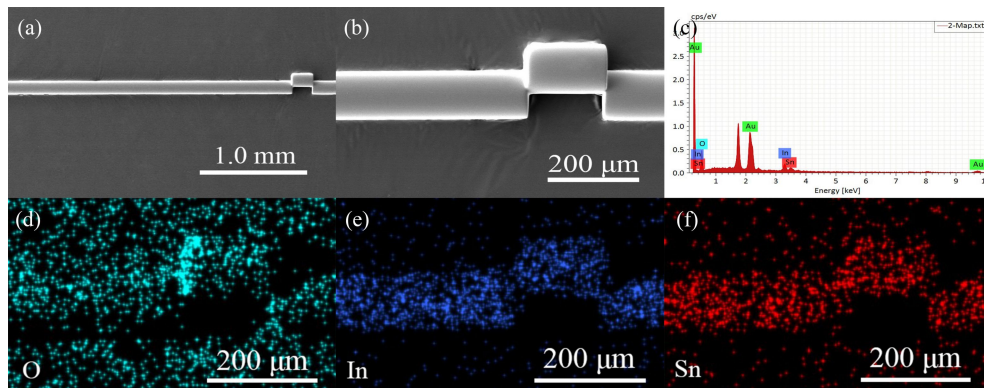

Fig. 3. The SEM images at different magnifications of the optical fiber FPI functionalized by ITO. (c) Elemental ratio of fiber surface. The EDS mapping images of (d) O, (e) In, and (f) Sn.

2.2 The principle of the optical fiber FPI conductivity sensor

In general, as a voltage is applied to the electrolyte solution, the anions and cations in the solution will move towards opposite electrodes as shown in Fig. 4(a). And an electric double layer (EDL) will form at the inter surface of the electrode and electrolyte solution which is several nanometers to tens of nanometers thick. In this experiment, results show that in region of the EDL between the transparent oxide electrode and the electrolyte, the conductivity of the electrolyte solution has a very significant effect on the refractive index of the electric double layer. Therefore, the conductivity of the electrolyte solution can be reflected by detecting the refractive index change in the EDL layer.
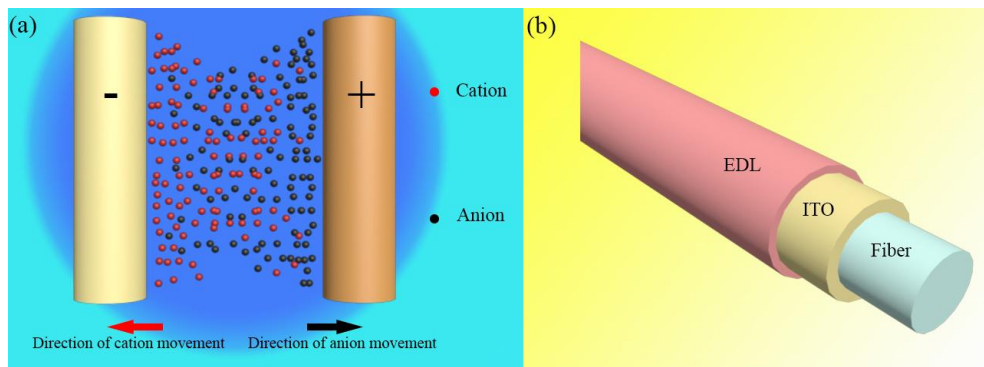

Fig. 4. Sensing principle diagram of the proposed sensor. (a) Anions and cations move to the poles. (b) EDL is formed on the surface of the optical fiber FPI functionalized by ITO.

When a voltage is applied to the ITO thin film functionalized optical fiber FPI, an electric double layer is formed on the surface of the optical fiber FPI [22, 26], as shown in Fig. 4(b). According to the formula:

$$I = I_1 + I_2 + 2\sqrt{I_1 I_2}\ \cos\left(\frac{4\pi n_{eff} L}{\lambda}\right) \tag{1}$$

Where I_1 and I_2 are the light intensity reflected the fiber through the first and second reflecting surfaces, respectively, λ is the wavelength of the incident light, n_{eff} is the effective refractive index of the substance in the open cavity of the FPI sensor, L is the cavity length of the FPI sensor. The change of the effective refractive index in the interference cavity will cause the center wavelength of the interference spectrum to shift. When the phase value in the cosine function bracket on the right side of Equation (1) is an odd multiple of π, the interference signal amplitude reaches its minimum value I_{min} (namely the trough), which can be expressed as:

$$\left(\frac{4\pi n_{eff} L}{\lambda_{vn}}\right) = (2n+1)\pi \tag{2}$$

Where, n is an integer and λ_{vn} is the central wavelength of the nth wave valley. When this large bias fiber FPI photoelectrode is used for conductivity monitoring, the change of the relative RI in the cavity caused by the EDL change will lead to the drift of the central wavelength λ_{vn} of the n order trough of the interference spectrum. When the RI in the cavity changes from n_{eff} to $n_{eff}+\Delta n_{eff}$, the phase value in the brackets of the cosine function on the right side of equation (1) corresponding to the n order trough is still $(2n+1)\pi$, and the central wavelength λ_{vn} of the n order trough will drift to $\lambda_{vn}+\Delta\lambda_{vn}$. So:

$$\left(\frac{4\pi n_{eff} L}{\lambda_{vn}}\right) = \frac{4\pi\left(n_{eff}+\Delta n_{eff}\right)L}{\lambda_{vn}+\Delta\lambda_{vn}} \tag{3}$$

So the sensitivity of refractive index change is

$$\Delta\lambda_{vn} / \Delta n_{eff} = \lambda_{vn} / n_{eff} \tag{4}$$

Equation (4) shows that the RI sensitivity of fiber FPI is determined by the chosen reflection interference valley λ_{vn} and the detected RI range, independent of the geometric length of the FPI cavity [28].

2.3 Construction of the experimental light path

Fig. 5 shows the experimental setup of the optical fiber FPI sensor functionalized by ITO electrode, and the illustration in the figure is a microscopic image of the optical fiber FPI. One end of the 3dB coupler is coupled with the F-P cavity sensing probe, and the other two ends are connected to an amplified spontaneous emission (ASE) light source and an optical spectrum analyzer (OSA, AQ-6317B). The sensor probe was placed in a specially designed test container in the laboratory during the test, and the sensor probe was fixed on the glass plate to eliminate tension crosstalk. A copper wire was connected to the surface of the ITO electrode with a silver paste. Then, the solution to be tested was injected into the chamber, and the entire F-P cavity was submerged. A DC power supply was connected to the transparent electrode ITO and solution waiting to be measured, respectively. The liquid temperature was controlled at 20°C throughout
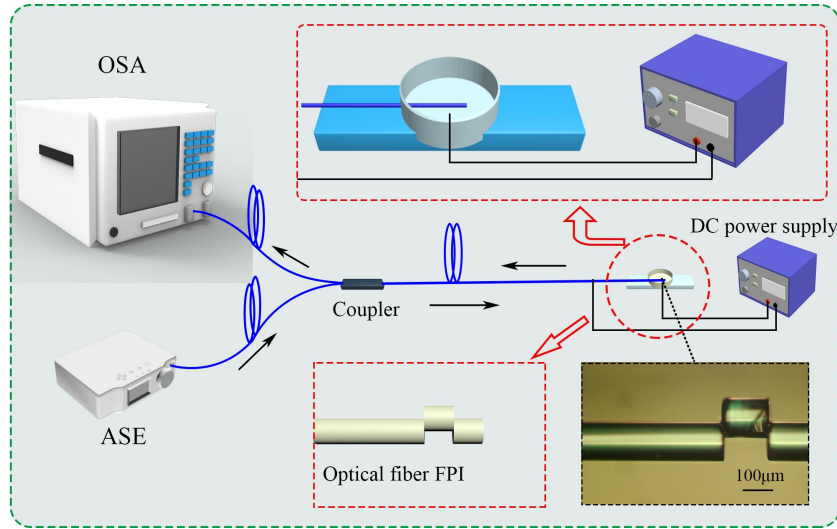
the experiment.

Fig. 5. Schematic diagram of conductivity detection of optical fiber FPI sensor functionalized by ITO. Inset: microscope image of optical fiber FPI functionalized by ITO.

3. Results and discussion

3.1 RI sensitivity characteristics of the optical fiber FPI functionalized by ITO

First, the RI sensitivity of fiber FPI optoelectrode was characterized. Optical fiber FPI was immersed in NaCl solutions with various concentrations at room temperature. The RI of the NaCl solutions varied in the range of 1.3370-1.3443, which was measured with an Abbe refractometer. Fig. 6(a) shows that with the increase of the RI, the optical fiber FPI spectral significantly shifted toward the long-wave direction with a maximum offset of 6.9 nm. As in Fig. 6(b), its RI sensitivity was approximately 965.46 nm/refractive index unit (RIU). And the optoelectrode has great RI sensitivity, the phase shift has a favorable linear relationship with the refractive index change, and the correlation coefficient is higher than 0.99.
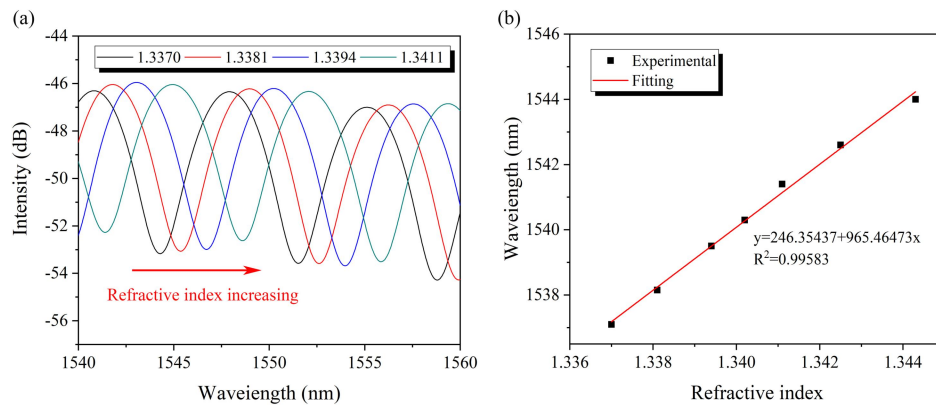

Fig. 6. (a) The interference spectrum moves when RI changes. (b) Fitting graph of RI sensitivity of the optical fiber FPI sensor.

3.2 Response of the optical fiber FPI sensor functionalized by ITO to conductivity

Next, the sensor was tested by immersing it in four KCl solutions. The concentration range of

KCl solution is 0.1-0.25 mol/L. The test results are shown in Fig. 7. Fig. 7(a)-(d) shows the interference spectrum of 0.1, 0.15, 0.2, and 0.25 mol/L KCl solution at different voltages. As the voltage gradually increases from 0 V to 0.5 V, the interference spectrum is gradually shifted toward the long-wave direction in Fig. 7. And the maximum phase shifts of the interference spectrum are 1.99, 2.59, 3.00, and 3.42 nm, respectively. In addition, from the Fig. 7, we found that when the same voltage is applied, the amount of spectral phase shift of FPI in electrolyte solutions with different concentrations is different. This is because the conductivities are different when the concentrations of the electrolyte solutions were changed. Then, we further study the relationship between the spectral phase shift and the electrical conductivity.
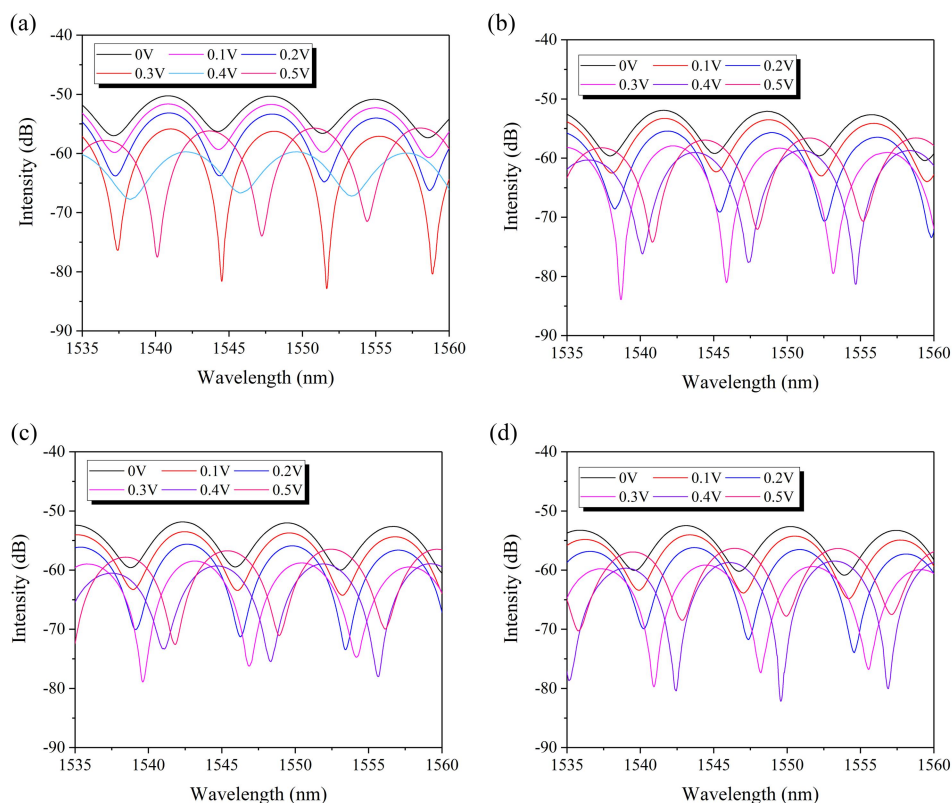

Fig. 7. The interference spectrum moves with the change of voltage in (a) 0.1 mol/L, (b) 0.15 mol/L, (c) 0.2 mol/L and (d) 0.25 mol/L KCl solution.

To further verify the relation between the spectral phase shift and the conductivity, the conductivities of the four KCl solutions were measured. In this concentration range, the conductivity increases with the increase in concentration. Then, multiple measurements were taken in 100 ml of the solution by a commercial conductivity meter and electrochemical workstation, respectively, as shown in Fig. 8. The conductivity of KCl solution with four concentrations was measured several times, as shown in Fig. 8(a). The measured conductivity values of 0.1, 0.15, 0.2, and 0.25 mol/L KCl solutions were 12.8987, 16.3387, 19.9212, and 24.7337 ms·cm^{-1}, respectively. In Fig. 8(b), the relative positions of Nyquist curves for different concentrations of KCl solutions are significantly different, and the relative position sequence is consistent with the test result of the conductivity meter. And, the result verifies the accuracy of the conductivity meter from the side.
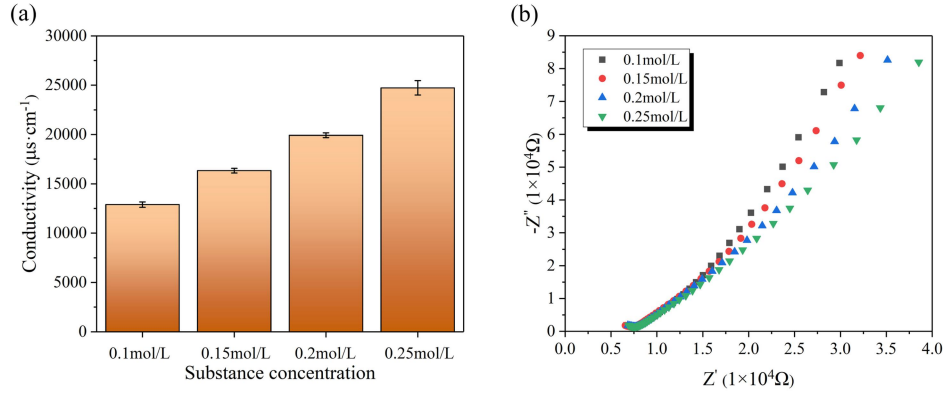
Fig. 8. (a) The conductivity of the solution is measured by a commercial conductivity meter. (b) Nyquist graph of KCl solution with different concentrations.

The fitting of interference wavelength shift and conductivity change under the same voltage excitation is shown in Fig. 9. The figure shows the phase shifts of electrolytes with different conductivities at multiple same voltages, respectively. We found all the lines show good linear relationship. Sensitivity is an important parameter to measure the performance of the sensor, reflecting the ability of the sensor to perceive small changes. The sensitivity of the optical fiber FPI sensor functionalized by ITO is defined as the slope of the linear fit. The performance of the sensor is slightly different when excited by different voltages. To compare the performance parameters of the sensor, the voltage, fitting function, sensitivity and R^2 of the optical fiber FPI sensor functionalized by ITO under different excitation voltages are listed, as shown in Table 1. As can be seen from the table, the sensor sensitivities increase with the excitation voltage. When the voltage is 0.1, 0.2, 0.3, 0.4, 0.5V, the sensitivity of the sensor is 0.0192, 0.0422, 0.1006, 0.1117, 0.1184 nm/ms·cm^{-1}, respectively. The maximum sensitivity was 0.1184 nm/ms·cm^{-1} at a voltage of 0.5V. This may be caused by different states of the EDL at different voltages. Currently, there is no clear conclusion on the effect of conductivity on the refractive index in the EDL layer. Here, we speculate here that within a certain voltage range, with the applied voltage, the EDL refractive index increases with the increase of electrical conductivity. Therefore, in the experiment, with the increase of the conductivity increases, the interference wavelength shift value reflecting this change increases.
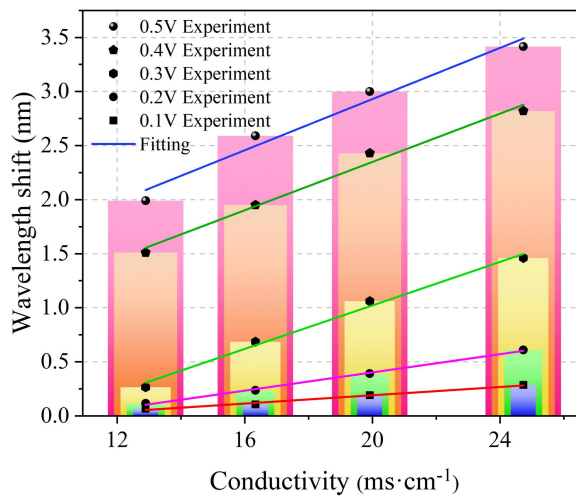

Fig. 9. Spectral shifts under different voltage excitations.

Table 1. Comparison of sensing performance under different voltage excitations.

Voltage	Fitting function	Sensitivity	R²
0.1V	y=0.0192x-0.19	0.0192 nm/ms·cm⁻¹	0.9913
0.2V	y=0.0422x-0.44	0.0422 nm/ms·cm⁻¹	0.9965
0.3V	y=0.1006x-0.99	0.1006 nm/ms·cm⁻¹	0.9919
0.4V	y=0.1117x+0.11	0.1117 nm/ms·cm⁻¹	0.9891
0.5V	y=0.1184x+0.56	0.1184 nm/ms·cm⁻¹	0.9864

3.3 Temperature response of FPI optoelectrode

The fabricated fiber FPI photoelectrode is fixed in the temperature chamber to test its temperature response. Fig. 10(a) shows the interference spectrum of the optoelectrode when the temperature varies from 20°C to 90°C. As can be seen from the figure, the interference spectral position almost does not change with temperature. The interference spectrum has slight intensity changes in some light bands, which may be caused by the airflow in the temperature chamber. As shown in the inset of the figure, the phase shift at the place with the largest intensity fluctuation is 0.1 nm. Then, we expand and analyze the troughs near 1550 nm, and obtain the relationship between temperature and spectral wavelength position as shown in Fig. 10(b). As can be seen from the figure, this fiber FPI optoelectrode is not sensitive to temperature changes. And the inserted spectra in the right top of Fig. 10 also show that the spectrum wavelength shift caused by temperature change is very little.

This temperature insensitive characteristic coincides with Wei et al's "Temperature insensitive miniaturized fiber inline Fabry–Perot interferometer for highly sensitive refractive index measurement" [27] and Yunjiang Rao et al's "High sensitivity gas refractometer based on all-fiber open-cavity Fabry–Perot interferometer formed by large lateral offset splicing" [28].
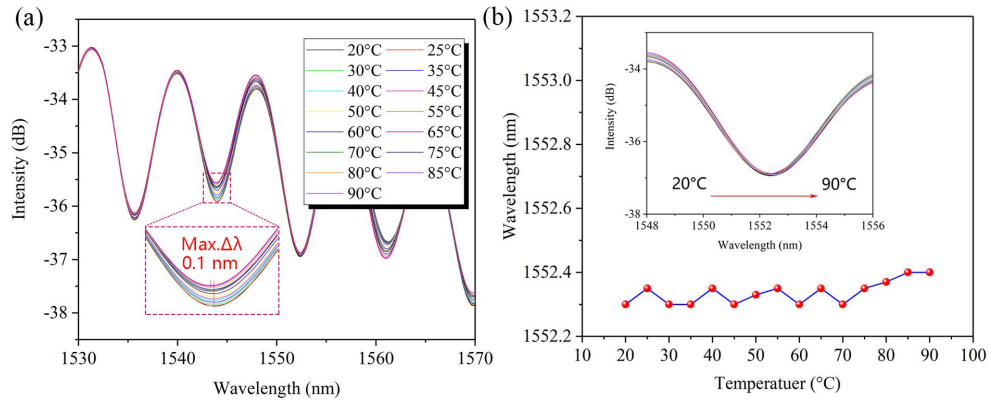

Fig. 10. (a) The reflection spectra of the tested fiber FPI optoelectrode at different temperatures. (b) Temperature induced fluctuates of spectrum valley center wavelength for the fiber FPI optoelectrode. Inset: It is the spectra near 1550 nm.

3.4 Repeatability and response time of the optoelectrode

To describe the repeatability and stability of the dynamic response for the device, real-time output intensity versus voltage variation was recorded. The output intensity tracking curve in 0.1

mol/L KCl solution is shown in Fig. 11(a). The intensity at 1543 nm was continuously recorded at the applied voltage of from 0 V to 0.3 V. The results show that the optoelectrode exhibits obvious repeatability. Fig. 11(b) illustrates the response time of the sensor, and its rising and falling times are 3.3 s and 3.6 s. For the conductivity sensor, the rising time and the falling time of one cycle may be caused by the movement time of anions and cations to the two electrodes. Here, the descending edge time is slightly greater than the ascending edge time. This may be because the voltage is unstable when the power supply is turned on, which causes the ions to move more slowly to the poles. In the subsequent work, we will optimize the experimental equipment to reduce the hysteresis time as much as possible. However, the response time of the photoelectrode is much lower than that of other similar electrodes (such as Electrical Double Layer Sensor stabilization time [29] and electrode adsorption time [30]).
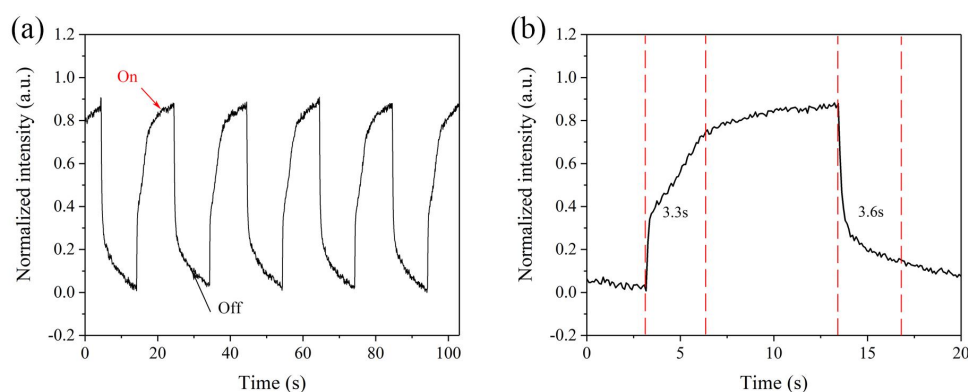

Fig. 11. (a) Dynamic response of the device when the power is periodically switched on and off. (b) Response time of the conductivity sensor.

4. Conclusions

In summary, a compact conductivity optoelectrode structure based on optical fiber is first proposed. ITO conductive layer was integrated with optical fiber FPI structure for aqueous solution conductivity measurement. The ITO was coated on the surface of the optical fiber FPI sensor and first used as an optoelectrode for detecting the conductivity of electrolyte solution. The sensor is based on the influence of the conductivity of the solution, which modulates the effective refractive index of the EDL. And the sensor has good repeatability, stability and fast response time. It is the first time to use interference spectrum and effective refractive index to obtain the conductivity information of solution, which provides a new method for conductivity detection. Importantly, the optical fiber FPI sensor functionalized with ITO interferometric photoelectrode has great development potential in biochemical analysis, biosensing, battery electrode surface monitoring and other fields.

Notes

Funding

Zhejiang Province of China (LGG20E040001).

References

[1] Chau, M. K.; Arega, N. G.; Tran, N. A. N.; Song, J.; Lee, S.; Kim, J.; Chung, M.; Kim, D. Capacitively coupled contactless conductivity detection for microfluidic capillary isoelectric focusing. *Anal. Chim. Acta* **2020**, *1124*, 60-70.

[2] Tuma; Petr Monitoring of biologically active substances in clinical samples by capillary and microchip electrophoresis with contactless conductivity detection: A review. *Anal. Chim. Acta* **2022**, *1225*, 340161.

[3] Coltro, W. K. T.; Neves, R. D.; Motheo, A. D.; da Silva, J. A. F.; Carrilho, E. Microfluidic devices with integrated dual-capacitively coupled contactless conductivity detection to monitor binding events in real time. *Sensor. Actuat. B-Chem.* **2014**, *192*, 239-246.

[4] Kuban, P.; Hauser, P. C. 20th anniversary of axial capacitively coupled contactless conductivity detection in capillary electrophoresis. *Trac-Trend. Anal. Chem.* **2018**, *102*, 311-321.

[5] Dvorak, M.; Rysava, L.; Kuban, P. Capillary Electrophoresis with Capacitively Coupled Contactless Conductivity Detection for Quantitative Analysis of Dried Blood Spots with Unknown Blood Volume. *Anal. Chem.* **2020**, *92*, 1557-1564.

[6] Zhao, Y. J.; Zhou, A.; Guo, H. Y.; Zheng, Z.; Xu, Y. M.; Zhou, C. M.; Yuan, L. B. An Integrated Fiber Michelson Interferometer Based on Twin-Core and Side-Hole Fibers for Multiparameter Sensing. *J. Lightwave Technol.* **2018**, *36*, 993-997.

[7] Jiang, P. Z.; Ouyang, Y.; Guo, H. Y.; Zhou, A. Highly sensitive torsion senor based on dual-side-hole fiber Mach-Zehnder interferometer. *Opt. Express* **2019**, *27*, 33881-33889.

[8] Lin, Z. T.; Zhao, Y.; Lv, R. Q.; Zheng, H. K.; Zhao, Q. High-sensitivity salinity sensor based on etched C-type micro-structured fiber sensing structure. *Sensor. Sensor Actuat A-Phys* **2022**, *339*, 113518.

[9] Peterson, J. I.; Vurek, G. G. Fiber-optic sensors for biomedical applications. *Science* **1984**, *224*, 123-127.

[10] Yang, X. H.; Yu, W. T.; Liu, Z. H.; Yang, J., Zhang, Y.; Kong, D.; Long, Q. L.; Yuan, T. T.; Cao, J. M.; Yuan, L. B.; Oh, K. Optofluidic twin-core hollowfiber interferometer for label-free sensing of the streptavidin-biotin binding. *Sensor. Actuat. B-Chem.* **2018**, *277*, 353-359.

[11] Pathak, A.; Gupta, B. D. Fiber-Optic Plasmonic Sensor Utilizing CTAB-Functionalized ZnO Nanoparticle-Decorated Carbon Nanotubes on Silver Films for the Detection of Catechol in Wastewater. *ACS Appl. Nano Mater.* **2020**, *3*, 2582-2593.

[12] Santos, J. S.; Raimundo, I. M.; Cordeiro, C. M. B.; Biazoli, C. R.; Gouveia, C. A. J.; Jorge, P. A. S. Characterisation of a Nafion film by optical fibre Fabry-Perot interferometry for humidity sensing. *Sensor. Actuat. B-Chem.* **2014**, *196*, 99-105.

[13] Warren-Smith, S. C.; Andre, R. M.; Dellith, J.; Eschrich, T.; Becker, M.; Bartelt, H. Sensing with ultra-short Fabry-Perot cavities written into optical micro-fibers. *Sensor. Actuat. B-Chem.* **2017**, *244*, 1016-1021.

[14] Hou, M. D.; Liang, X. Y.; Zhang, T. T.; Qiu, C. Y.; Chen, J. D.; Liu, S. D.; Wang, W. J.; Fan, X. D. DNA Melting Analysis with Optofluidic Lasers Based on Fabry-Perot Microcavity. *ACS Sensors* **2018**, *3*, 1750-1755.

[15] Zhu, C.; Perman, J. A.; Gerald, R. E.; Ma, S. Q.; Huang, J. Chemical Detection Using a Metal-Organic Framework Single Crystal Coupled to an Optical Fiber. *ACS Appl. Mater. Inter.* **2019**, *11*, 4393-4398.

[16] Wang, X. D.; Wolfbeis, O. S. Fiber-Optic Chemical Sensors and Biosensors (2015-2019). *Anal. Chem.* **2020**, *92*, 397-430.

[17] Ouyang, Y.; Xu, X. F.; Zhao, Y. J.; Zhou, A.; Yuan, L. B. Temperature Compensated Refractometer Based on Parallel Fiber Fabry-Perot Interferometers. *IEEE Photonics Technol. Lett.* **2018**, *30*, 1262-1265.

[18] Teng, P. P.; Jiang, Y. H.; Chang, X. Y.; Shen, Y.; Liu, Z. H.; Copner, N.; Yang, J.; Li, K.; Bowkett, M.; Yuan, L. B.; Yang, X. H. Highly sensitive on-line detection of trace Pb^{2+} based on tapered fiber integrated with black phosphorus. *Opt. Fiber Technol.* **2021**, *66*, 102668.

[19] Zhou, L.; Liu, C.; Sun, Z. B.; Mao, H. J.; Zhang, L.; Yu, X. F.; Zhao, J. L.; Chen, X. F. Black phosphorus based fiber optic biosensor for ultrasensitive cancer diagnosis. *Biosens. Bioelectron.* **2019**, *137*, 140-147.

[20] Sansone, L.; Malachovska, V.; La Manna, P.; Musto, P.; Borriello, A.; De Luca, G.; Giordano, M. Nanochemical fabrication of a graphene oxide-based nanohybrid for label-free optical sensing with fiber optics. *Sensor. Actuat. B-Chem.* **2014**, *202*, 523-526.

[21] Xu, B.; Huang, J.; Xu, X. F.; Zhou, A.; Ding, L. Y. Ultrasensitive NO Gas Sensor Based on the Graphene Oxide-Coated Long-Period Fiber Grating. *ACS Appl. Mater. Inter.* **2019**, *11*, 40868-40874.

[22] Chen, Z. L.; Song, C. Y.; Sun, X. W.; Guo, H. F.; Zhu, G. D. Kinetic and isotherm studies on the electrosorption of NaCl from aqueous solutions by activated carbon electrodes. *Desalination* **2011**, *267*, 239-243.

[23] Oldham, K. B. A Gouy-Chapman-Stern model of the double layer at a (metal)/(ionic liquid) interface. *J. Electroanal. Chem.* **2008**, *613*, 131-138.

[24] Nie, B. Q.; Xing, S. Y.; Brandt, J. D.; Pan, T. R. Droplet-based interfacial capacitive sensing. *Lab Chip* **2012**, *12*, 1110-1118.

[25] Chang, Y.; Wang, L.; Li, R. Y.; Zhang, Z. C.; Wang, Q.; Yang, J. L.; Guo, C. F.; Pan, T. R. First Decade of Interfacial Iontronic Sensing: From Droplet Sensors to Artificial Skins. *Adv. Mater.* **2020**, *33*, 2003464.

[26] Mariani, S.; Strambini, L. M.; Barillaro, G. Electrical double Layer-Induced ion surface accumulation for ultrasensitive refractive index sensing with nanostructured porous silicon interferometers. *ACS Sensors* **2018**, *3*, 595-605.

[27] Wei, T.; Han, Y. K.; Li, Y. J.; Tsai, H. L.; Xiao, H. Temperature-insensitive miniaturized fiber inline Fabry-Perot interferometer for highly sensitive refractive index measurement. *Opt. Express* **2008**, *16*, 5764-5769.

[28] Duan, D. W.; Rao, Y. J.; Zhu, T. High sensitivity gas refractometer based on all-fiber open-cavity Fabry-Perot interferometer formed by large lateral offset splicing. *J. Opt. Soc. Am. B.* **2012**, *29*, 912-915.

[29] Liu, Y. L.; Shen, J. Y.; Chu, F. J.; Zeng, X. Y.; Pandey, R.; Li, M. L.; Xiao, J. L.; Luo, J. K.; Wang, X. Z.; Zhang, L. Electrical double layer-based iontronic sensor for detection of electrolytes concentration. *Chin. J. Anal. Chem.* **2022**, *50*, 13-19.

[30] Wang, Y.; Wang, R. G.; Xu, S. C.; Liu, Q.; Wang, J. X. Polypyrrole/polyaniline composites with enhanced performance for capacitive deionization. *Desalin. Water Treat.* **2015**, *54*, 3248-3256.